The current issue and full text archive of this journal is available on Emerald Insight at:
https://www.emerald.com/insight/0332-1649.htm

A robust numerical method for drawing the fluid flux-barrier geometry in the inner and outer rotor radial flux synchronous reluctance machines based on the finite difference method

Received 22 March 2022
Revised 24 August 2022
2 September 2022
Accepted 2 September 2022

Ali Jamali Fard
Electrical Machines and Transformer Research Laboratory (EMTRL), Amirkabir University of Technology, Tehran, Iran and Department of Electrical Engineering, Amirkabir University of Technology, Tehran, Iran, and

Mojtaba Mirsalim
Electrical Machines and Transformer Research Laboratory (EMTRL), Amirkabir University of Technology, Tehran, Iran; Department of Electrical Engineering, Amirkabir University of Technology, Tehran, Iran and Engineering Department, St. Mary's University, San Antonio, Texas, USA

Abstract

Purpose – Rotor shape optimization is crucial in designing synchronous reluctance machines (SynRMs) because the machine performance is directly proportional to the rotor's magnetic saliency ratio. The rotor geometry in synchronous reluctance machines is complex, and many geometrical parameters must be optimized. When fluid flux-barrier geometry is desirable, using analytic equations to prepare the rotor geometry for finite element analysis could be tedious. This paper aims to provide a robust numerical procedure to draw the fluid flux-barrier geometry in transversally laminated radial flux inner and outer rotor ŞynRMs by directly solving the magnetic vector potential equation using the finite difference method.

Design/methodology/approach – In this paper, the goal is to have a robust procedure for drawing the rotor geometry for an arbitrary number of slots (Ns), poles (p) and flux-barrier layers (Nfb). Therefore, this paper targeted several combinations to investigate the performance of the proposed algorithm. The MATLAB software is used to implement the proposed algorithm. The ANSYS Maxwell software is used for counterpart finite element simulation to check the correctness of the results derived by the proposed method.

Findings – Several inner and outer rotor SynRMs considering a different number of poles and a different number of flux-barrier layers per pole are studied to investigate the performance of the proposed algorithm. Results corresponding to each case are presented, and it is shown that the method is robust, flexible and fast enough, which could be used for the generation of the rotor geometry for the finite element analysis effectively.

Originality/value – The value of the proposed algorithm is its simplicity and straightforwardness in its implementation for the preparation of the rotor geometry with the desired fluid flux-barrier layer curvature resolution suitable for the finite element analysis. The procedure presented in this paper is based on the ideal magnetic loading concept, and in future works, a similar idea could be used for linear and axial flux SynRMs.

Keywords Synchronous reluctance machines (SynRMs), Magnetic vector potential (MVP) equation, Finite difference method (FDM), Electrical machines

Paper type Research paper

COMPEL - The international journal for computation and mathematics in electrical and electronic engineering
© Emerald Publishing Limited
0332-1649
DOI 10.1108/COMPEL-03-2022-0123

1. Introduction

Synchronous reluctance machines (SynRMs) are gaining more attention in applications requiring high dynamics, high torque density and fault-tolerant capabilities, such as traction and household appliances (Bianchi *et al.*, 2022; López-Torres *et al.*, 2018). Robust rotor structure, absence of rotor joule loss, low cost and convenience in manufacturing are the advantages of a SynRM (Cai *et al.*, 2016; Wang *et al.*, 2015). As the SynRM rotor is made of iron lamination, no brushes/slip-rings and expensive permanent magnets are needed (Cai *et al.*, 2014, 2016). Although electrical machines with rare-earth permanent magnets have high performance, the high cost and the insufficiency of rare-earth permanent magnet materials will be obstacles to further development in applications such as electric vehicles or hybrid electric vehicles (Liu *et al.*, 2016; López-Torres *et al.*, 2018). Line-start synchronous reluctance motors are also a suitable alternative to induction motors in fixed-speed direct-on-line applications such as pumps and fans (Baka *et al.*, 2021; Hu *et al.*, 2022).

In a SynRM, the total developed electromagnetic torque is the reluctance type. Therefore, the rotor shape optimization is crucial in designing SynRMs because the machine performance is directly proportional to the rotor's magnetic saliency ratio. In the case of an improper design, a SynRM presents some drawbacks, such as a high torque ripple and a low-power factor (Bianchi *et al.*, 2022; Cai *et al.*, 2014). The rotor geometry in SynRMs is complex, and many geometrical parameters are involved (Bacco and Bianchi, 2019). Several flux-barrier layers per pole should be taken into account to achieve a good magnetic saliency ratio (Wang *et al.*, 2017; Guan *et al.*, 2016). This, in turn, makes the rotor optimization process a difficult task because in an optimization problem, when the number of decision variables is high, the number of objective function calls increases.

Figure 1 shows some possible rotor topologies to generate reluctance torque for a continuous rotation. As you can see, these structures aim to generate an appropriate non-uniform permeability distribution in the rotor to generate reluctance torque. Figure 1(a) represents the rotor geometry of a switched reluctance machine. In this machine, the rotor magnetic anisotropy is achieved by salient poles. Figures 1(b) and 1(c) show two topologies possible for SynRMs. The SynRM's smoothly rotating field distinguished it from switched reluctance machine (Miller *et al.*, 1991).

The structure shown in Figure 1(b) is called transversally laminated anisotropy (TLA) structure because the staking direction is axial. The staking of the rotor shown in Figure 1(c) is in the radial direction, and it is known as axially laminated anisotropy (ALA) structure. The most appealing feature of the ALA rotor construction is the opportunity to significantly increase the number of flux-barrier layers per pole, making it possible to significantly boost the magnetic saliency of the rotor. This elevated saliency, in turn, increases the machine's power factor and, potentially, its efficiency by lowering the required stator current. Unfortunately, the ALA

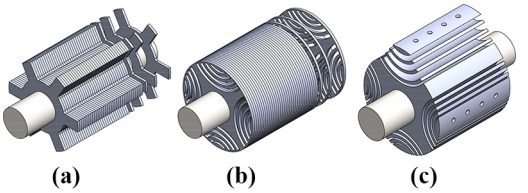

Figure 1.
Some possible rotor topologies for radial-flux reluctance machines

Note: (a) Salient pole anisotropy; (b) transversally laminated anisotropy; and (c) axially laminated anisotropy

structure is vulnerable to elevated iron losses in the rotor laminations close to the air gap, limiting its efficiency advantages. Perhaps even more importantly, the significant manufacturability challenges associated with the axially laminated rotor construction have seriously hindered its commercialization opportunities (Pellegrino *et al.*, 2016).

This work focuses on TLA structure (more common because of the manufacturing feasibility). For a TLA rotor structure, several geometries are possible (Figure 2). Segmented, circular and fluid flux-barrier geometries are explained in Pellegrino *et al.* (2016). In general, there are two ways to specify the geometry of a flux-barrier layer [however, a combination is also possible (Bianchi *et al.*, 2016)]:

(1) predefined methods (segmented, circular, etc.); and

(2) methods based on the magnetic (fluid) flux lines.

In the first method, the designer defines a fully constrained geometry for flux-barrier layers. In this case, adequate geometrical constraints should be considered to avoid infeasible cases during the rotor shape optimization process. Other reasonable conditions, which will not influence the machine performance, are also necessary to decrease the number of design parameters to simplify the optimization process (Guan *et al.*, 2016). Figures 2(a) and 2(b) depict two models of this category.

In the second method, the geometry of rotor flux-barrier layers is determined by knowing the information of magnetic flux lines. In this case, flux-barrier layers are parallel with magnetic flux lines to achieve a high rotor magnetic saliency ratio. A closed-form expression of the magnetic flux lines inside the rotor can be derived from the conformal mapping theory and the Joukowski air-flow potential formulation (Pellegrino *et al.*, 2016). However, the generation of the rotor geometry using complex analytic equations of the Joukowski method is complicated. This formulation was originally developed to describe the fluid flow paths channeled by two infinite plates forming an angle π/p, and with a plug of radius, centered

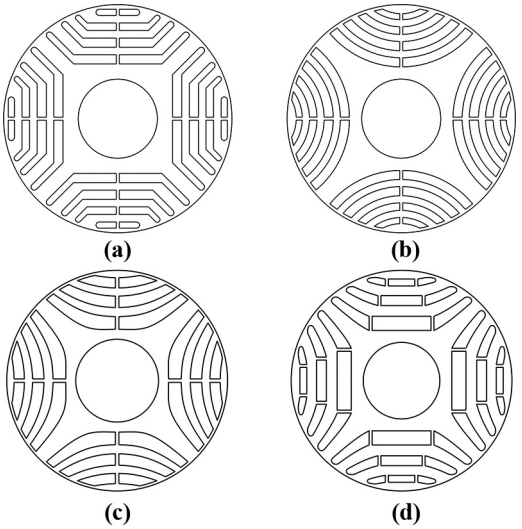

Notes: (a) Segmented; (b) circular; (c) magnetic (fluid) flux-barrier; (d) combined

Figure 2.
Different rotor geometries of synchronous reluctance machines

into the origin of the reference frame. However, this method does not provide a good insight for an electric machine designer.

In this paper, we introduce a new methodology for calculating the geometry of the flux-barrier layers. The proposed method is based on the ideal magnetic loading concept in alternating currents (AC) machines and a numeric method [finite difference method (FDM)] instead of the analytic methods to draw the rotor geometry with a desirable geometry resolution.

2. Proposed method

2.1 Magnetic vector potential equation

A four-pole inner rotor SynRM and a ten-pole outer rotor SynRM are shown in Figure 3. Flux lines illustrated in this figure are calculated due to the excitation of the stator winding when there is no flux-barrier layer in the rotor. The flux lines pattern inside the solid rotor could be used as an indication of the optimal flux-barrier geometry. Flux lines are contour lines of the magnetic vector potential (MVP). Because the maximum variation in the value of the MVP occurs on a path perpendicular to the flux lines, we have the maximum magneto-motive force drop on the same path. Therefore, flux-barrier edges should be in parallel with flux lines (as shown in Figure 2b) to minimize the d-axis flux lines distortion and effectively block the q-axis ones with a beneficial effect on the rotor anisotropy (Bianchi *et al.*, 2022).

As you can see in Figure 3, for both inner and outer rotor machines, for the derivation of flux-barrier layers geometry, we should solve the MVP equation in a hollow cylinder as shown in Figure 4. For a magnetic domain with a linear permeability and without free currents, the MVP equation is as follows (Jackson, 1999):

$$\nabla^2 \mathbf{A} = 0 \tag{1}$$

In our case, the focus is on one axial cross-section of the machine. Therefore, the problem is a two-dimensional problem, and we only have A_z component; consequently:

$$\nabla^2 A_z = 0 \tag{2}$$

Equation (2) is Laplace equation which in a cylindrical coordinate system is as follows (Bastos and Sadowski, 2003):

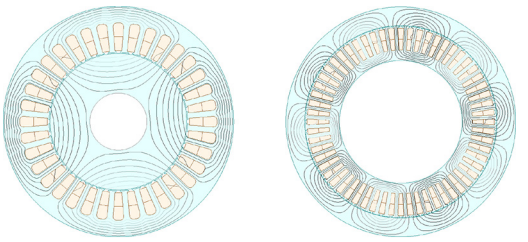

(a) **(a)**

Notes: (a) Inner rotor; (b) outer rotor

Figure 3.
Flux lines due to the excitation of the stator winding considering a solid rotor

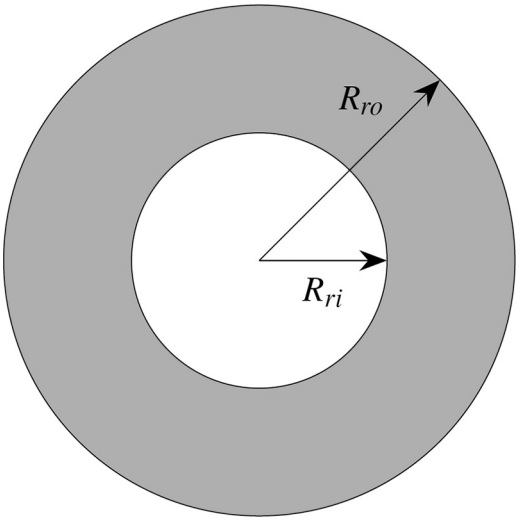

Notes: R_{ri}: inner rotor radius; $R_\{ro\}$: outer rotor radius

Figure 4.
Solid rotor geometry and its dimensions

$$\frac{\partial^2 A_z}{\partial r^2} + \frac{1}{r}\frac{\partial A_z}{\partial r} + \frac{1}{r^2}\frac{\partial^2 A_z}{\partial \theta^2} + \frac{\partial^2 A_z}{\partial z^2} = 0 \tag{3}$$

Here r, θ and z are radial, circumferential and axial components of the coordinate system. A_z is a scalar field. Because the value of A_z along the axial direction is constant, its derivative with respect to z equals 0. Therefore, we have:

$$\frac{\partial^2 A_z}{\partial r^2} + \frac{1}{r}\frac{\partial A_z}{\partial r} + \frac{1}{r^2}\frac{\partial^2 A_z}{\partial \theta^2} = 0 \tag{4}$$

A_z is a function of r and θ. Equipotential flux lines are contour lines of this function. Therefore, for the calculation of flux lines in the hollow cylinder, at first, we should calculate $A_z(r,\theta)$ by solving equation (4) and then finding its contour lines.

2.2 Boundary conditions

The geometry of our interest is a hollow cylinder in which two boundary conditions should be specified. The first one is on its inner surface, and the second one is on its outer surface. The solution variable A_z is calculated by knowing the value of the normal and tangential components of the flux density on boundaries. The flux density is equal to the curl of the MVP, mathematically:

$$\mathbf{B} = \nabla \times \mathbf{A} \tag{5}$$

The curl of A in the cylindrical coordinate system is as follows:

$$\nabla \times \mathbf{A} = \frac{1}{r} \times \begin{vmatrix} \hat{r} & r\hat{\theta} & \hat{z} \\ \frac{\partial}{\partial r} & \frac{\partial}{\partial \theta} & \frac{\partial}{\partial z} \\ A_r & rA_\theta & A_z \end{vmatrix} \tag{6}$$

Because the only non-zero component of $\mathbf{A}$ is A_z, we have:

$$\mathbf{B} = \nabla \times \mathbf{A} = \frac{1}{r} \times \begin{vmatrix} \hat{r} & r\hat{\theta} & \hat{z} \\ \frac{\partial}{\partial r} & \frac{\partial}{\partial \theta} & \frac{\partial}{\partial z} \\ 0 & 0 & A_z \end{vmatrix} = \frac{1}{r}\frac{\partial A_z}{\partial \theta}\,\hat{r} - \frac{\partial A_z}{\partial r}\,\hat{\theta} \tag{7}$$

According to equation (7), the radial component of flux density is equal:

$$B_r = \frac{1}{r}\frac{\partial A_z}{\partial \theta} \tag{8}$$

In a radial flux AC machine, the interest is having a sinusoidal distribution of the flux density in the middle of the air gap. For an ideal p-pole machine, the radial component of flux density as a function of circumferential coordinate in the middle of the air gap is equal to:

$$B_r(\theta) = B_p \times \sin\left(\frac{p}{2}\theta\right) \tag{9}$$

where B_p is the peak value of the flux density in the middle of the air gap. Combining equations (8) and (9), we have:

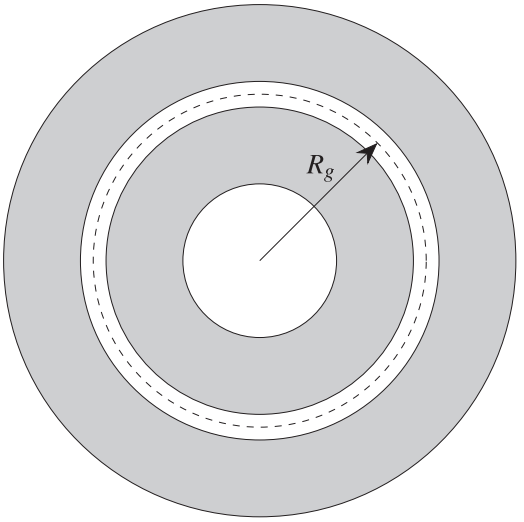

Figure 5.
Air gap radius

$$B_r(\theta) = B_p \times \sin\left(\frac{p}{2}\theta\right) = \frac{1}{R_g}\frac{\partial A_z}{\partial \theta} \tag{10}$$

where R_g is the air gap radius as shown is Figure 5. For inner rotor machines, the air gap radius is almost equal to R_{ro}, and for the outer rotor machines, it is almost equal to R_{ri}. If we integrate equation (10), then we can calculate A_z as follows:

$$A_z = -\frac{2}{p} \times R_g \times B_p \times \cos\left(\frac{p}{2}\theta\right) \tag{11}$$

Equation (11) is used for determining the value of A_z on the outer surface of inner rotor machines and the inner surface of outer rotor machines. The second boundary condition is the zero-vector potential boundary condition. It is used to confine the magnetic flux inside the rotor. Table 1 summarizes boundary conditions for inner and outer rotor machines.

2.3 Mesh

Figure 6 shows an example of the solution mesh. In this example, the number of mesh layers in the radial direction equals six. The mesh nodes are equally spaced in both radial and

Boundary	Inner rotor	Outer rotor
Inner surface	$A_z = 0$	$A_z = -\frac{2}{p} \times R_{ri} \times B_p \times \cos\left(\frac{p}{2}\theta\right)$
Outer surface	$A_z = -\frac{2}{p} \times R_{ro} \times B_p \times \cos\left(\frac{p}{2}\theta\right)$	$A_z = 0$

Table 1. Boundary conditions for inner rotor and outer rotor machines

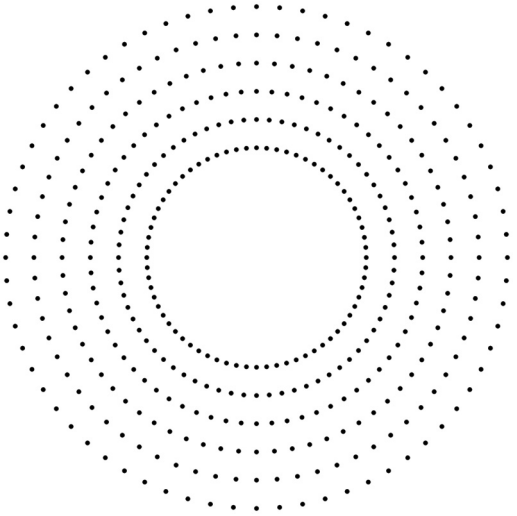

Figure 6. An example of the solution mesh

circumferential directions. The number of mesh layers in the radial direction is N_r, and the number of mesh layers in the circumferential direction is N_t. Therefore, the total number of mesh nodes equals $N_r \times N_t$. After generating the mesh, we should assign an index to each mesh node. Indexing starts from innermost to outermost mesh layers by moving counterclockwise on each mesh layer. The coordinate of the first mesh node is $(R_{ri}, 0)$. The mesh indexing pattern is shown in Figure 7.

The accuracy and smoothness of calculated flux lines depend on the values of N_t and N_r. To properly determine the values of N_t and N_r, we define the rotor geometry resolution (RGR) parameter. The RGR equals the maximum radial or circumferential distance between two adjacent mesh nodes. The circumferential angular distance between two adjacent nodes of a mesh layer is equal to:

$$\Delta\theta = \frac{2\pi}{N_t} \tag{12}$$

The maximum circumferential distance between two adjacent mesh is for two mesh nodes which belong to the outermost layer, and it is equal to:

$$R_{ro} \times \Delta\theta \tag{13}$$

The distance between two adjacent mesh nodes in the radial direction is equal to:

$$\Delta r = \frac{R_{ro} - R_{ri}}{N_r - 1} \tag{14}$$

According to equations (13) and (14), the RGR is equal to:

$$RGR = \max(R_{ro} \times \Delta\theta, \Delta r) \tag{15}$$

RGR is one of the MATLAB program inputs. After setting the value of RGR, we can calculate N_t and N_r as follows:

$$R_{ro} \times \Delta\theta \leq RGR \Rightarrow R_{ro} \times \frac{2\pi}{N_t} \leq RGR \Rightarrow N_t = \text{Ceil}\left(\frac{2\pi R_{ro}}{RGR}\right) \tag{16}$$

The ceil function is used to fix the value of N_t. Similarly, for N_r, we have:

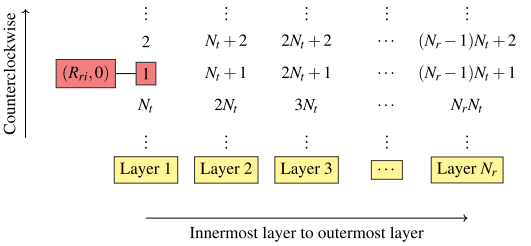

Figure 7.
Indexing pattern of mesh nodes

$$\Delta r \le RGR \Rightarrow \frac{R_{ro} - R_{ri}}{N_r - 1} \le RGR \Rightarrow N_r = \text{Ceil}\left(\frac{R_{ro} - R_{ri}}{RGR} + 1\right) \tag{17}$$

By knowing the values of N_t and N_r, we can calculate Δr and $\Delta\theta$, and finally, we can calculate the coordinates of each mesh node. The value of radial coordinate of i-th mesh layer nodes is equal to:

$$r_i = R_{ri} + i \times \Delta r, \qquad i = 0, 1, \cdots, (N_r - 1) \tag{18}$$

And the value of circumferential coordinate of the j-th node of a mesh layer is equal to:

$$\theta_j = j \times \Delta\theta, \qquad j = 0, 1, \cdots, (N_t - 1) \tag{19}$$

The relationship between mesh node index and its coordinates is as follows:

$$\text{Node index} = i \times N_t + j + 1 \Longleftrightarrow (r_i, \theta_j) = \text{Node coordinates} \tag{20}$$

2.4 System of equations

As described in the mesh section, the total number of mesh nodes equals $N_r \times N_t$. Already we know the value of A_z for innermost and outermost mesh layers from boundary conditions. Therefore, the total number of unknowns is equal to $N_{r-2} \times N_t$. We should have $N_{r-2} \times N_t$ linearly independent equations to calculate the value of A_z for all inner mesh nodes uniquely. Figure 8 represents an internal mesh node with its neighboring points.

There are three differential terms in equation (4). The first term could be discretized using the second-order difference equation (Morton and Mayers, 2005):

$$\frac{\partial^2 A_z}{\partial r^2} \simeq \frac{A_z^{\text{Front}} - 2A_z^{\text{Inner}} + A_z^{\text{Rear}}}{(\Delta r)^2} \tag{21}$$

The second term could be approximated by central difference method:

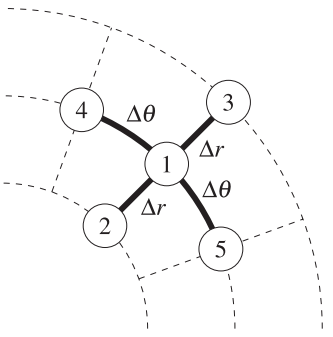

Notes: (1) Inner; (2) rear; (3) front; (4) left; (5) right

Figure 8. An internal mesh node and its neighboring points

$$\frac{1}{r}\times\frac{\partial A_z}{\partial r}\simeq\frac{1}{r^{\text{Inner}}}\times\frac{A_z^{\text{Front}}-A_z^{\text{Rear}}}{2\Delta r} \tag{22}$$

where r^{Inner} is the radius of inner point. The third term is discretized like the first term:

$$\frac{1}{r^2}\times\frac{\partial^2 A_z}{\partial\theta^2}\simeq\frac{1}{\left(r^{\text{Inner}}\right)^2}\times\frac{A_z^{\text{Left}}-2A_z^{\text{Inner}}+A_z^{\text{Right}}}{\left(\Delta\theta\right)^2} \tag{23}$$

Therefore, for each inner mesh node, we can write following equation:

$$c_1A_z^{\text{Inner}}+c_2A_z^{\text{Rear}}+c_3A_z^{\text{Front}}+c_4A_z^{\text{Left}}+c_5A_z^{\text{Right}}=0 \tag{24}$$

where:

$$\begin{cases} c_1 = & -\dfrac{2}{\left(\Delta r\right)^2}-\dfrac{2}{\left(r^{\text{Inner}}\right)^2\times\left(\Delta\theta\right)^2} \\ c_2 = & \dfrac{1}{\left(\Delta r\right)^2}-\dfrac{1}{2\times r^{\text{Inner}}\times\Delta r} \\ c_3 = & \dfrac{1}{\left(\Delta r\right)^2}+\dfrac{1}{2\times r^{\text{Inner}}\times\Delta r} \\ c_4 = & \dfrac{1}{\left(r^{\text{Inner}}\right)^2\times\left(\Delta\theta\right)^2} \\ c_5 = & \dfrac{1}{\left(r^{\text{Inner}}\right)^2\times\left(\Delta\theta\right)^2} \end{cases} \tag{25}$$

When calculating the coefficients of equation (24) using equation (25), we can construct the matrix equation (26). The left-hand matrix (stiffness matrix) in equation (26) is sparse, and we used MATLAB sparse matrix package to assemble and solve it. The code is pretty fast and can generate the rotor geometry with the desired accuracy instantly.

Figure 9 shows an internal mesh node, with its corresponding relationship as depicted in equation (26). After solving matrix equation (26), we can have the value of A_z for each mesh nodes. Therefore, one can calculate the value of A_z for any arbitrary point inside the rotor by two-dimensional interpolation:

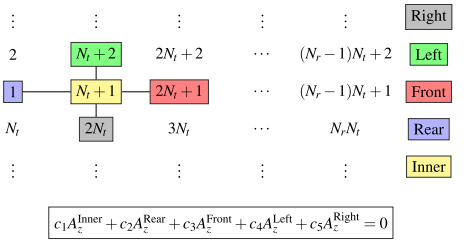

Figure 9.
An internal mesh node, the corresponding equation for this mesh node is shown in equation (26)

$$
\begin{bmatrix}
1 & 0 & \cdots & 0 & 0 & 0 & \cdots & 0 & 0 & 0 & \cdots & 0 & \cdots & 0 & 0 & \cdots & 0 \\
0 & 1 & \cdots & 0 & 0 & 0 & \cdots & 0 & 0 & 0 & \cdots & 0 & \cdots & 0 & 0 & \cdots & 0 \\
\vdots & \vdots & \ddots & \vdots & \vdots & \vdots & \ddots & \vdots & \vdots & \vdots & \ddots & \vdots & \ddots & \vdots & \vdots & \ddots & \vdots \\
0 & 0 & \cdots & 1 & 0 & 0 & \cdots & 0 & 0 & 0 & \cdots & 0 & \cdots & 0 & 0 & \cdots & 0 \\
c_2^{N_t+1} & 0 & \cdots & 0 & c_1^{N_t+1} & c_4^{N_t+1} & \cdots & c_5^{N_t+1} & c_3^{N_t+1} & 0 & \cdots & 0 & \cdots & 0 & 0 & \cdots & 0 \\
0 & c_2^{N_t+2} & \cdots & 0 & c_5^{N_t+2} & c_1^{N_t+2} & \cdots & 0 & 0 & c_3^{N_t+2} & \cdots & 0 & \cdots & 0 & 0 & \cdots & 0 \\
\vdots & \vdots & \ddots & \vdots & \vdots & \vdots & \ddots & \vdots & \vdots & \vdots & \ddots & \vdots & \ddots & \vdots & \vdots & \ddots & \vdots \\
0 & 0 & \cdots & c_2^{2N_t} & c_4^{2N_t} & 0 & \cdots & c_1^{2N_t} & 0 & 0 & \cdots & c_3^{2N_t} & \cdots & 0 & 0 & \cdots & 0 \\
0 & 0 & \cdots & 0 & c_2^{2N_t+1} & 0 & \cdots & 0 & c_1^{2N_t+1} & c_4^{2N_t+1} & \cdots & c_5^{2N_t+1} & \cdots & 0 & 0 & \cdots & 0 \\
0 & 0 & \cdots & 0 & 0 & c_2^{2N_t+2} & \cdots & 0 & c_5^{2N_t+2} & c_1^{2N_t+2} & \cdots & 0 & \cdots & 0 & 0 & \cdots & 0 \\
\vdots & \vdots & \ddots & \vdots & \vdots & \vdots & \ddots & \vdots & \vdots & \vdots & \ddots & \vdots & \ddots & \vdots & \vdots & \ddots & \vdots \\
0 & 0 & \cdots & 0 & c_4^{3N_t} & 0 & \cdots & c_2^{3N_t} & 0 & 0 & \cdots & c_1^{3N_t} & \cdots & 0 & 0 & \cdots & 0 \\
\vdots & \vdots & \ddots & \vdots & \vdots & \vdots & \ddots & \vdots & \vdots & \vdots & \ddots & \vdots & \ddots & \vdots & \vdots & \ddots & \vdots \\
0 & 0 & \cdots & 0 & 0 & 0 & \cdots & 0 & 0 & 0 & \cdots & 0 & \cdots & 1 & 0 & \cdots & 0 \\
0 & 0 & \cdots & 0 & 0 & 0 & \cdots & 0 & 0 & 0 & \cdots & 0 & \cdots & 0 & 1 & \cdots & 0 \\
\vdots & \vdots & \ddots & \vdots & \vdots & \vdots & \ddots & \vdots & \vdots & \vdots & \ddots & \vdots & \ddots & \vdots & \vdots & \ddots & \vdots \\
0 & 0 & \cdots & 0 & 0 & 0 & \cdots & 0 & 0 & 0 & \cdots & 0 & \cdots & 0 & 0 & \cdots & 1
\end{bmatrix}
\begin{bmatrix}
A_z^1 \\ A_z^2 \\ \vdots \\ A_z^{N_t} \\ A_z^{N_t+1} \\ A_z^{N_t+2} \\ \vdots \\ A_z^{2N_t} \\ A_z^{2N_t+1} \\ A_z^{2N_t+2} \\ \vdots \\ A_z^{3N_t} \\ \vdots \\ A_z^{(N_r-1)N_t+1} \\ A_z^{(N_r-1)N_t+2} \\ \vdots \\ A_z^{N_rN_t}
\end{bmatrix}
=
\begin{bmatrix}
A_z^{IBC,1} \\ A_z^{IBC,2} \\ \vdots \\ A_z^{IBC,N_t} \\ \boxed{0} \\ 0 \\ \vdots \\ 0 \\ 0 \\ 0 \\ \vdots \\ 0 \\ \vdots \\ A_z^{OBC,1} \\ A_z^{OBC,2} \\ \vdots \\ A_z^{OBC,N_t}
\end{bmatrix}
\tag{26}
$$

In equation (26), the value of A_z for the innermost mesh layer nodes is equal to:

$$A_z^i = A_z^{IBC,i}, \qquad i = 1, 2, \cdots, N_t \tag{27}$$

where *IBC* stands for inner boundary condition. For inner rotor machines, we have:

$$A_z^{IBC,i} = 0 \tag{28}$$

And based on the ideal magnetic loading concept, for outer rotor machines, we have:

$$A_z^{IBC,i} = -\frac{2}{p} \times R_{ri} \times B_p \times \cos\left(\frac{p}{2} \times (i-1) \times \Delta\theta\right) \tag{29}$$

Similarly, the value of A_z for the outermost mesh layer nodes is equal to:

$$A_z^{(N_r-1)N_t+i} = A_z^{OBC,i}, \qquad i = 1, 2, \cdots, N_t \tag{30}$$

where *OBC* stands for outer boundary condition. For inner rotor machines, we have:

$$A_z^{OBC,i} = -\frac{2}{p} \times R_{ro} \times B_p \times \cos\left(\frac{p}{2} \times (i-1) \times \Delta\theta\right) \tag{31}$$

And for outer rotor machines:

$$A_z^{OBC,i} = 0 \tag{32}$$

2.5 Per-unit model

Figure 10 shows the rotor of a four-pole SynRM. In this example, the number of flux-barrier layers per pole is three. Geometrical parameters are as follows (Collection I):

$$\{R_{ri}, R_{ro}, w_{trib}, w_{rrib1}, w_{rrib2}, w_{rrib3}, w_{ry1}, w_{ry2}, w_{ry3}, w_{ry4}, d_{b1}, d_{b2}, d_{b3}\} \tag{33}$$

where:

w_{trib} = width of the tangential rib;
w_{rribk} = width of the k-th radial rib (k = 1,2,. . ., N_{fb});
w_{ryk} = width of the k-th rotor yoke (flux-carrier) (k = 1,2,. . ., $N_{\text{fb}} + 1$); and
d_{bk} = depth of the k-th flux-barrier (k = 1,2,. . ., N_{fb}).

The width of the tangential rib is constant for all flux-barrier layers. However, the width of radial ribs could be different. Although the number of rotor geometrical parameters is equal to 13 for this example, the number of independent variables is equal to 12 because we have the following constraint:

$$w_{ry1} + w_{ry2} + w_{ry3} + w_{ry4} + d_{b1} + d_{b2} + d_{b3} = R_{ro} - R_{ri} \tag{34}$$

The constraint shown in equation (34) could be restated in another form by definition of the air insulation ratio (K_{air}):

$$K_{\text{air}} = \frac{\sum_{i=1}^{3} d_{bi}}{\sum_{i=1}^{4} w_{ryi} + \sum_{i=1}^{3} d_{bi}} = \frac{\sum_{i=1}^{3} d_{bi}}{w_{ry} + \sum_{i=1}^{3} d_{bi}} \tag{35}$$

where w_{ry} is the total rotor yoke thickness in alignment with the rotor q-axis:

$$w_{ry} = w_{ry1} + w_{ry2} + w_{ry3} + w_{ry4} \tag{36}$$

The per-unit rotor model was introduced in Jamali Fard and Mirsalim (2022) to simplify the optimization process and geometrical calculations. One benefit of working with the per-unit rotor model is scaling. When optimization is done for a specific motor rating, it can be scaled up or down for other ratings with little effort.

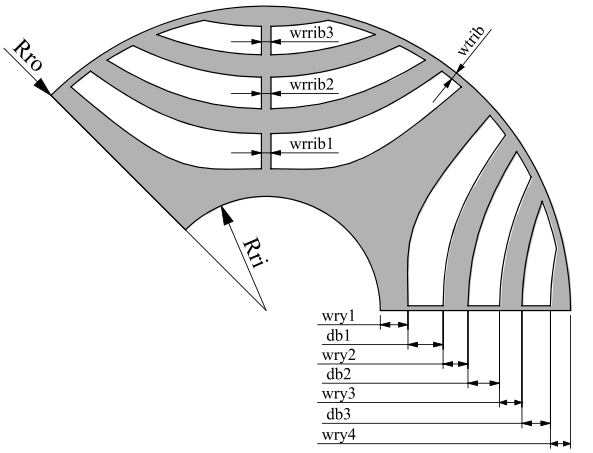

Figure 10.
The rotor of a four-pole synchronous reluctance machine with three flux-barrier layers per pole and its geometrical parameters

The same logic is used in this work. The rotor yokes per-unit variables are defined as follows (Jamali Fard and Mirsalim, 2022):

$$\begin{cases} \gamma_{wry2} = \dfrac{w_{ry2}}{w_{ry1}} \leq 1 \\ \gamma_{wry3} = \dfrac{w_{ry3}}{w_{ry2}} \leq 1 \\ \gamma_{wry4} = \dfrac{w_{ry4}}{w_{ry3}} \leq 1 \end{cases} \tag{37}$$

And per-unit variables related to the depth of flux-barrier layers are (Jamali Fard and Mirsalim, 2022):

$$\begin{cases} \gamma_{db2} = \dfrac{w_{ry2}}{w_{ry1}} \leq 1 \\ \gamma_{db3} = \dfrac{w_{ry3}}{w_{ry2}} \leq 1 \end{cases} \tag{38}$$

Regarding definitions of K_{air}, w_{ry} and per-unit variables, we can rewrite Collection I in the following form (Collection II):

$$\{R_{ri}, R_{ro}, w_{trib}, w_{rrib1}, w_{rrib2}, w_{rrib3}, K_{\text{air}}, \gamma_{wry2}, \gamma_{wry3}, \gamma_{wry4}, \gamma_{db2}, \gamma_{db3}\} \tag{39}$$

All variables in Collection II are independent. The advantage of using Collection II instead of Collection I is avoiding geometrical errors when changing the rotor dimensions during the optimization. Because variables introduced in Collection II are per unit, we have a good indication of their values. The following matrix equation shows the relationship between per-unit values and actual values:

$$\begin{bmatrix} 1 & 1 & 1 & 1 & 0 & 0 & 0 \\ \gamma_{wry2} & -1 & 0 & 0 & 0 & 0 & 0 \\ 0 & \gamma_{wry3} & -1 & 0 & 0 & 0 & 0 \\ 0 & 0 & \gamma_{wry4} & -1 & 0 & 0 & 0 \\ 0 & 0 & 0 & 0 & 1 & 1 & 1 \\ 0 & 0 & 0 & 0 & \gamma_{db2} & -1 & 0 \\ 0 & 0 & 0 & 0 & 0 & \gamma_{db3} & -1 \end{bmatrix} \begin{bmatrix} w_{ry1} \\ w_{ry2} \\ w_{ry3} \\ w_{ry4} \\ d_{b1} \\ d_{b2} \\ d_{b3} \end{bmatrix} = \begin{bmatrix} (1 - K_{\text{air}}) \times (R_{ro} - R_{ri}) \\ 0 \\ 0 \\ 0 \\ K_{\text{air}} \times (R_{ro} - R_{ri}) \\ 0 \\ 0 \end{bmatrix} \tag{40}$$

Because flux lines are contour lines of the function $A_z(r, \theta)$, we should have an adequate methodology to calculate the contour line passing through a desired point inside the rotor to draw the flux-barrier layers. For example, for the innermost flux-barrier layer of an inner rotor motor, we should find two contour lines passing through these two base points (cartesian coordinates are given):

$$\begin{cases} \text{Point } 1 = \left(R_{ri} + w_{ry1}, \dfrac{w_{rrib1}}{2}\right) \\ \text{Point } 2 = \left(R_{ri} + w_{ry1} + d_{b1}, \dfrac{w_{rrib1}}{2}\right) \end{cases} \tag{41}$$

We used MATLAB software to implement the proposed method. The inputs are variables of Collection II, and outputs are segmented polylines describing the geometry of flux-barrier layers. The smoothness of these polylines is determined by the proper setting of the value of *RGR*.

3. Results and discussion

A simulation is performed to investigate the correctness of the solutions generated by the proposed method. A four-pole inner rotor SynRM is considered, and a sinusoidal flux density distribution with the peak value equal to 0.7 T (Tesla) is assumed on its outer

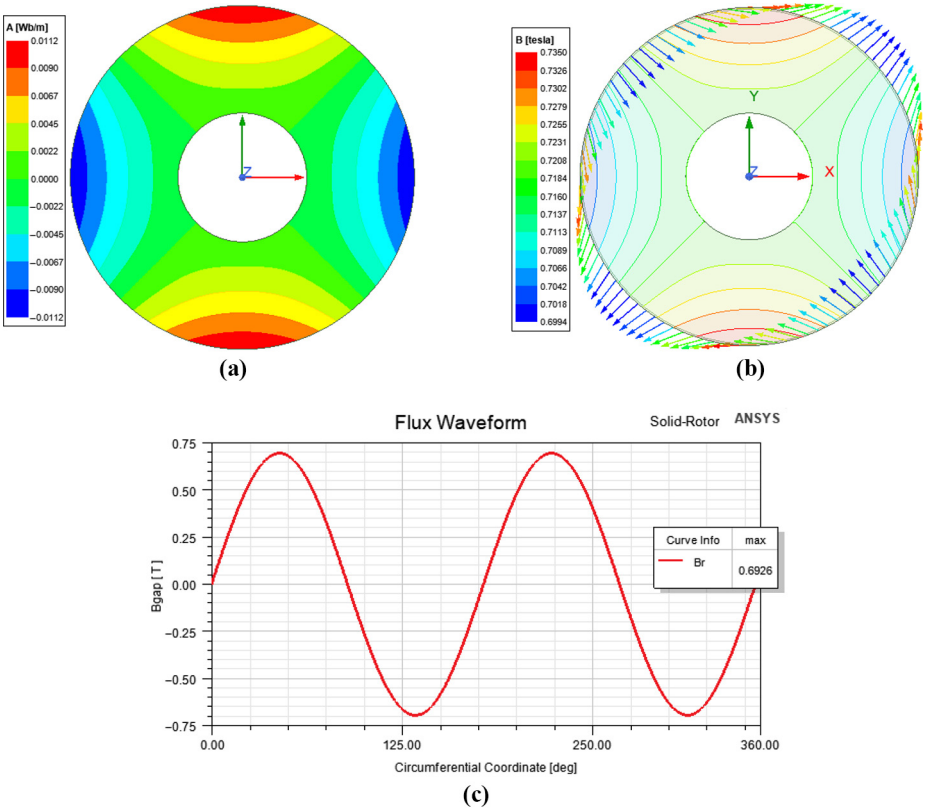

Figure 11.
Calculation of flux lines inside the solid rotor for an inner rotor, four-pole machine by the finite element method

Notes: (a) Magnetic vector potential; (b) flux density vectors on outer rotor surface; (c) the radial component of the flux density on the outer rotor surface as a function of the circumferential coordinate

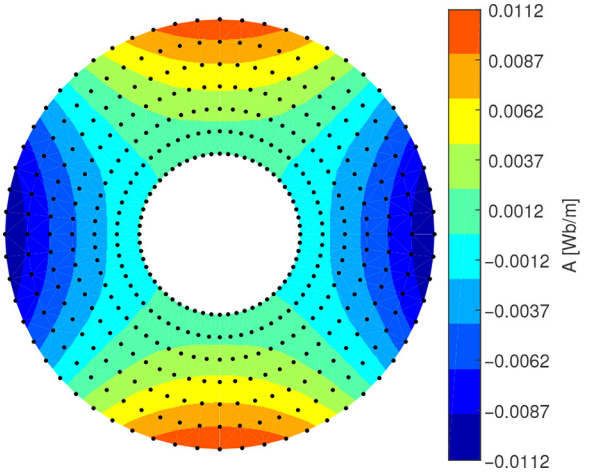

Figure 12.
Magnetic vector potential distribution inside the solid rotor for an inner rotor, four-pole machine by proposed method

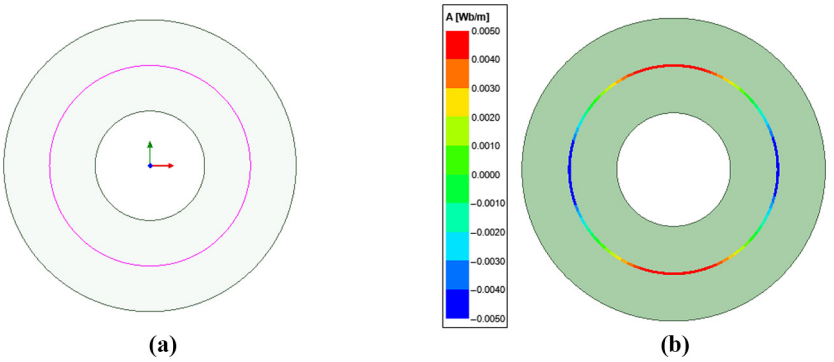

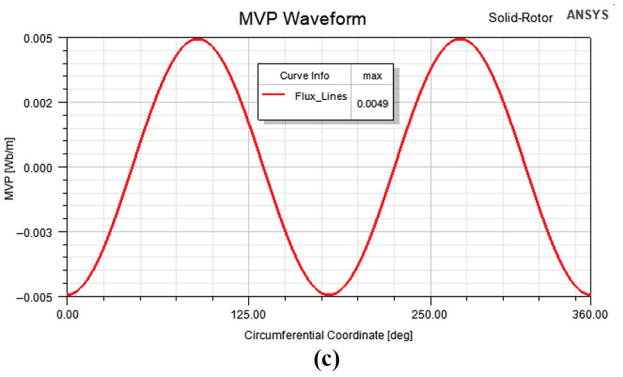

Figure 13.
Calculation of the magnetic vector potential on the candidate circle inside the solid rotor for an inner rotor, four-pole machine by the finite element method

Notes: (a) Candidate circle; (b) magnetic vector potential distribution; (c) magnetic vector potential waveform on the candidate circle as a function of the circumferential coordinate

surface. Figure 11 illustrates the finite element analysis results. We used the ANSYS Maxwell software for the finite element analysis. Figure 11(a) shows the MVP distribution inside the rotor. As one can see, the maximum value of MVP is equal to 0.0112 Wb/m. Figure 11(b) represents the flux density vectors on the outer surface of the rotor. As can be seen, the peak value of the radial component of the flux density is equal to 0.7 T. However, the maximum value of the flux density amplitude could be higher than 0.7 T. Figure 11(c)

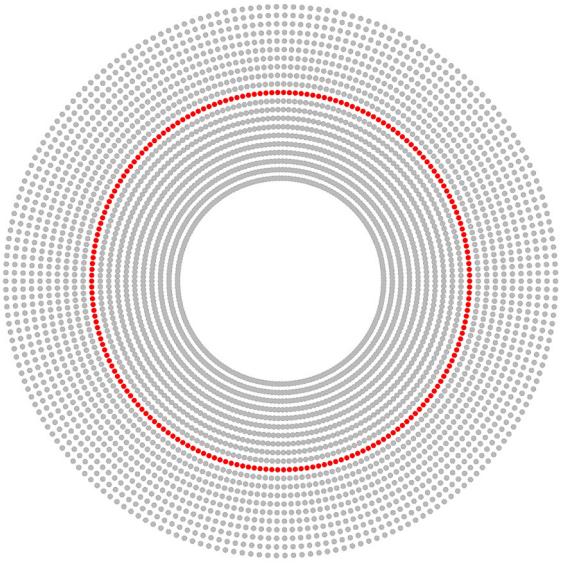

(a)

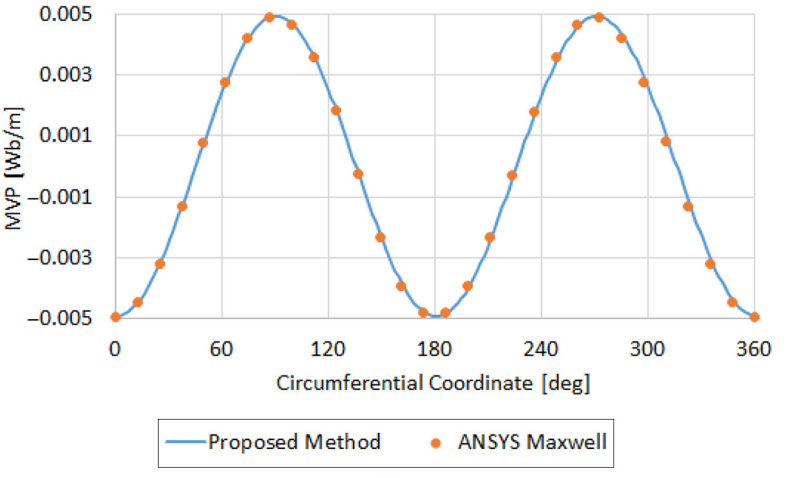

(b)

Figure 14.
Comparison of the magnetic vector potential waveform derived by the proposed method and the waveform calculated by the finite element analysis software

Notes: (a) Candidate mesh points; (b) magnetic vector potential waveforms

depicts the variation of the radial component of the flux density versus the circumferential component. As we expected, it is purely sinusoidal, and its peak value is equal to 0.7 T.

Figure 12 shows the MVP distribution calculated by the proposed method for the same case shown in Figure 11. As it is seen, the result is close to Figure 11(a) which validates the correctness of solutions generated by the proposed method. The maximum value of MVP by the proposed method is equal to 0.0112 Wb/m which is the same as what we calculated using ANSYS Maxwell software.

For a better comparison, we considered a candidate circle in the middle of the rotor [Figure 13(a)] and calculated the value of MVP on it. Figure 13(b) shows the MVP distribution on the candidate circle, and Figure 13(c) shows the MVP waveform as a function of circumferential coordinate. Figure 14(a) represents the candidate mesh points of the

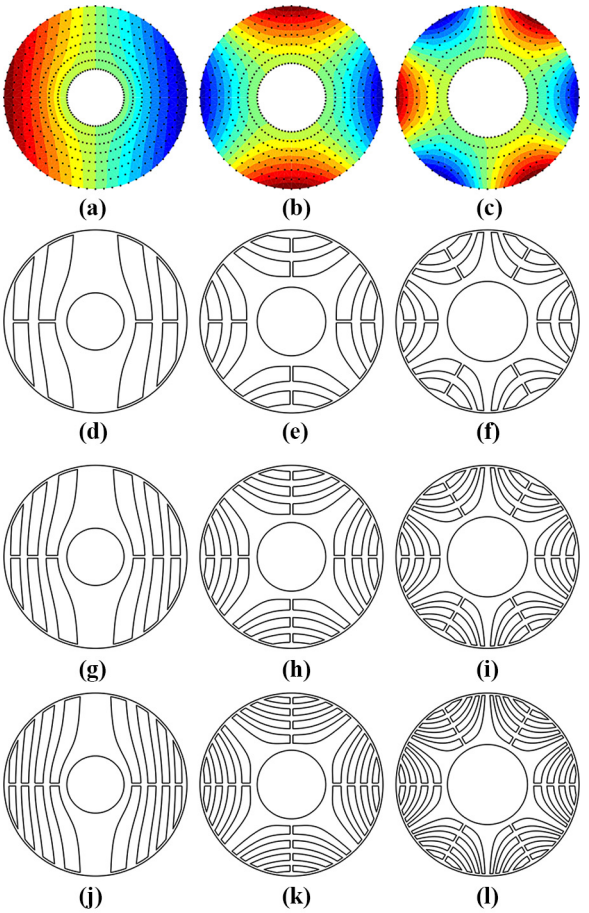

Notes: (a) $p = 2$; (b) $p = 4$; (c) $p = 6$; (d) $N_{fb} = 2$; (e) $N_{fb} = 2$; (f) $N_{fb} = 2$; (g) $N_{fb} = 3$; (h) $N_{fb} = 3$; (i) $N_{fb} = 3$; (j) $N_{fb} = 4$; (k) $N_{fb} = 4$; (l) $N_{fb} = 4$

Figure 15.
The rotor geometry of the three inner rotor synchronous reluctance machines considering the different number of flux-barrier layers derived by the proposed method

proposed method for comparison of their values with the finite element analysis result. The waveforms of both methods are given in Figure 14(b) in the same chart. As it is seen, we have a good match between the two methods that validates the correctness of the proposed method.

The advantage of the proposed method is in using the FDM to solve the MVP equation. Because the mesh is predefined, the meshing time is negligible. By properly setting the value of *RGR*, a fine and uniform mesh could be generated. Finally, contour lines can be calculated with arbitrary smoothness.

The slot/pole combination selection is always a challenging problem in the design of synchronous electric machines. This problem is even more difficult for SynRMs because the number of flux-barrier layers is added to the slot/pole combination (Wang *et al.*, 2022). Several combinations should be studied to find a proper combination for a specific design.

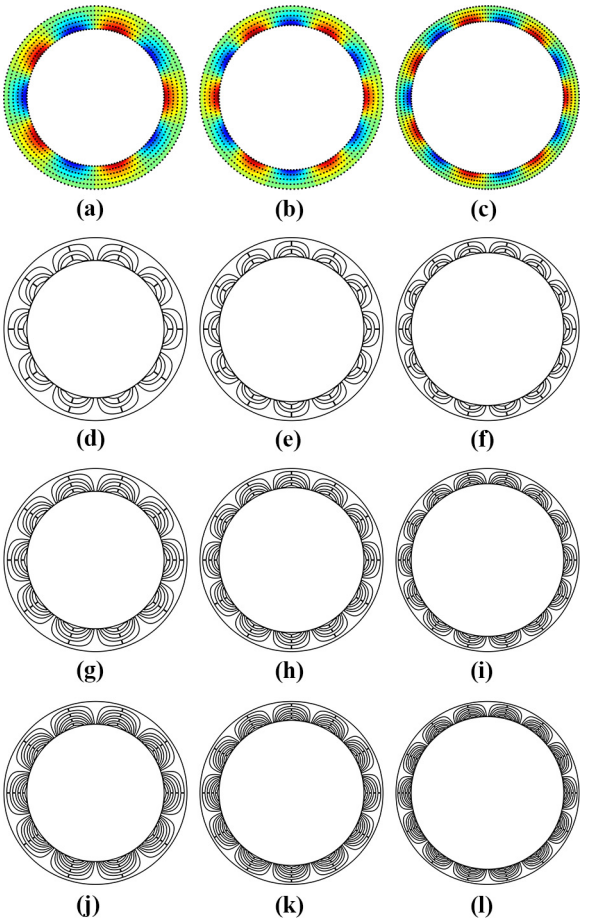

Notes: (a) $p = 10$; (b) $p = 12$; (c) $p = 14$; (d) $N_{fb} = 2$; (e) $N_{fb} = 2$; (f) $N_{fb} = 2$; (g) $N_{fb} = 3$; (h) $N_{fb} = 3$; (i) $N_{fb} = 3$; (j) $N_{fb} = 4$; (k) $N_{fb} = 4$; (l) $N_{fb} = 4$

Figure 16.
The rotor geometry of the three outer rotor synchronous reluctance machines considering the different number of flux-barrier layers derived by the proposed method

The proposed method should be able to generate the rotor geometry for any arbitrary combination.

To evaluate the performance of the proposed method, we considered several p-N_{fb} combinations for both inner and outer rotor SynRMs. Figure 15 shows the rotor geometries derived by the proposed method of the three inner rotor SynRMs considering different numbers of flux-barrier layers. The value of per-unit variables for generating these geometries are as follows:

$$K_{\mathrm{air}} = 0.5, \qquad \gamma_{wry2} = \gamma_{wry3} = \gamma_{wry4} = \gamma_{db2} = \gamma_{db3} = 0.9 \tag{42}$$

Figure 16 illustrates the rotor geometries of the three outer rotor SynRMs considering different numbers of flux-barrier layers. According to the results, the method is robust enough for the generation of different rotor geometries considering arbitrary p-N_{fb} combination. After the geometry generation by the proposed method, further modifications could be used to modify the geometry of the end flux-barrier.

4. Conclusion

A robust numerical procedure for drawing the fluid flux-barrier geometry in the inner and outer rotor radial flux SynRMs was presented in this paper. The method is based on the ideal magnetic loading concept and uses the FDM to solve the MVP equation. Several cases, including the inner and outer rotor machines, were studied to investigate the algorithm's performance. According to the results, the method can generate the rotor geometry for an arbitrary slot, pole and flux-barrier layer combination with the desired fluid flux-barrier layer curvature resolution suitable for the finite element analysis. The advantage of the proposed algorithm is its simplicity and straightforwardness in its implementation for the generation of the rotor geometry suitable for optimization.

References

Bacco, G. and Bianchi, N. (2019), "Design criteria of flux-barriers in synchronous reluctance machines", *IEEE Transactions on Industry Applications*, Vol. 55 No. 3, pp. 2490-2498.

Baka, S., Sashidhar, S. and Fernandes, B.G. (2021), "Design of an energy efficient line-start two-pole ferrite assisted synchronous reluctance motor for water pumps", *IEEE Transactions on Energy Conversion*, Vol. 36 No. 2, pp. 961-970.

Bastos, J.P.A. and Sadowski, N. (2003), *Electromagnetic Modeling by Finite Element Methods*, CRC press.

Bianchi, N., Babetto, C. and Bacco, G. (2022), *Synchronous Reluctance Machines: Analysis, Optimization and Applications*, IET, available at: https://shop.theiet.org/

Bianchi, N., Bolognani, S., Carraro, E., Castiello, M. and Fornasiero, E. (2016), "Electric vehicle traction based on synchronous reluctance motors", *IEEE Transactions on Industry Applications*, Vol. 52 No. 6, pp. 4762-4769.

Cai, H., Guan, B., Xu, L. and Choi, W. (2014), "Optimal design of synchronous reluctance machine", *COMPEL: The International Journal for Computation and Mathematics in Electrical and Electronic Engineering*, Vol. 33 No. 5, pp. 1569-1586, doi: 10.1108/COMPEL-09-2013-0287.

Cai, S., Jin, M.-J., Hao, H. and Shen, J.-X. (2016), "Comparative study on synchronous reluctance and pm machines", *COMPEL: The International Journal for Computation and Mathematics in Electrical and Electronic Engineering*, Vol. 35 No. 2, pp. 607-623, doi: 10.1108/COMPEL-12-2015-0447.

Guan, Y., Zhu, Z.Q., Afinowi, I.A.A., Mipo, J.C. and Farah, P. (2016), "Design of synchronous reluctance and permanent magnet synchronous reluctance machines for electric vehicle application",

COMPEL: The International Journal for Computation and Mathematics in Electrical and Electronic Engineering, Vol. 35 No. 2, pp. 586-606, doi: 10.1108/COMPEL-02-2015-0109.

Hu, Y., Chen, B., Xiao, Y., Shi, J., Li, L. and Li, X. (2022), "Rotor design and optimization of the three-phase line-start synchronous reluctance motor", *2019 22nd International Conference on Electrical Machines and Systems (ICEMS)*, pp. 1-6.

Jackson, J.D. (1999), *Classical Electrodynamics*, American Association of Physics Teachers.

Jamali Fard, A. and Mirsalim, M. (2022), "Proposing a sequential iterative method based on a per-unit model for rotor shape optimization in permanent magnet assisted synchronous reluctance motors", *COMPEL – The International Journal for Computation and Mathematics in Electrical and Electronic Engineering*, Vol. 41 No. 5, pp. 1826-1848, doi: 10.1108/COMPEL-09-2021-0340.

Liu, X.L.Y., Liu, Z., Ling, T. and Luo, Z. (2016), "Analysis and design of a high power density permanent magnet-assisted synchronous reluctance machine with low-cost ferrite magnets for EVS/HEVS", *COMPEL – The International Journal for Computation and Mathematics in Electrical and Electronic Engineering*, Vol. 35 No. 6, pp. 1949-1964, doi: 10.1108/COMPEL-05-2016-0233.

López-Torres, C., Garcia, A., Riba, J., Lux, G. and Romeral, L. (2018), "Computationally efficient design and optimization approach of PMA-SYNRM in frequent operating torque – speed range", *IEEE Transactions on Energy Conversion*, Vol. 33 No. 4, pp. 1776-1786.

Miller, T.J.E., Hutton, A., Cossar, C. and Staton, D.A. (1991), "Design of a synchronous reluctance motor drive", *IEEE Transactions on Industry Applications*, Vol. 27 No. 4, pp. 741-749.

Morton, K.W. and Mayers, D.F. (2005), *Numerical Solution of Partial Differential Equations: An Introduction*, Cambridge University Press, Cambridge.

Pellegrino, G., Jahns, T.M., Bianchi, N., Soong, W.L. and Cupertino, F. (2016), *The Rediscovery of Synchronous Reluctance and Ferrite Permanent Magnet Motors: Tutorial Course Notes*, Springer Nature, Switzerland.

Wang, Y., Bacco, G. and Bianchi, N. (2017), "Geometry analysis and optimization of pm-assisted reluctance motors", *IEEE Transactions on Industry Applications*, Vol. 53 No. 5, pp. 4338-4347.

Wang, K., Zhu, Z.Q., Ombach, G., Koch, M., Zhang, S. and Xu, J. (2015), "Torque ripple reduction of synchronous reluctance machines", *COMPEL: The International Journal for Computation and Mathematics in Electrical and Electronic Engineering*, Vol. 34 No. 1, pp. 3-17, doi: 10.1108/COMPEL-11-2013-0366.

Wang, K., Zhu, Z.Q., Ombach, G., Koch, M., Zhang, S. and Xu, J. (2022), "Optimal slot/pole and flux-barrier layer number combinations for synchronous reluctance machines", *2013 Eighth International Conference and Exhibition on Ecological Vehicles and Renewable Energies (EVER)* pp. 1-8.

Further reading

Woodson, H.H. and Melcher, J.R. (1968), *Electromechanical Dynamics*, John Wiley and Sons, Hoboken.

Corresponding author

Ali Jamali Fard can be contacted at: a.jamalifard@aut.ac.ir

For instructions on how to order reprints of this article, please visit our website:
www.emeraldgrouppublishing.com/licensing/reprints.htm
Or contact us for further details: **permissions@emeraldinsight.com**